ELSEVIER

Contents lists available at ScienceDirect

Journal of Alloys and Compounds

journal homepage: www.elsevier.com/locate/jalcom



Silver-nanoclusters boosted bifunctional hybrid catalysis for ampere-hour-scale zinc-air batteries

Tong Liu^a, Degui Li^c, Xiangqun Zhuge^a, Zhihong Luo^d, Yaming Pang^a, Kun Luo^{a,*}, Yurong Ren^a, Mehmet Onur Aydogdu^e, Mohan Edirisinghe^{e,*}, Guogang Ren^{b,*}

- ^a Jiangsu Province Engineering Research Centre of Intelligent Manufacturing Technology for the New Energy Vehicle Power Battery, School of Materials Science and Engineering, Changzhou University, Changzhou 213164, PR China
- ^b University of Hertfordshire, Hatfield, Hertfordshire AL10 9AB, UK
- ^c School of Materials Science and Engineering, Baise University, Baise 533000, PR China
- ^d College of Materials Science and Engineering, Guilin University of Technology, Guilin 541004, PR China
- e Department of Mechanical Engineering, University College London, London WC1E 7JE, UK

ARTICLE INFO

Keywords: ORR OER Ag nanoclusters Carbon nanoframes Zinc air batteries

ABSTRACT

Rechargeable zinc-air batteries (ZABs) reveal compelling potential in energy storage systems. However, slow kinetics in oxygen reduction and oxygen evolution reactions (ORR/OER) severely constrain the practical deployment of ZABs. To overcome these issues, a heterogeneous bifunctional catalyst: Nano-silver cluster-enhanced nickel-iron-layered double hydroxide/cobalt, nitrogen-codoped carbon nano-frames structure (Ag-NiFe-LDH/Co-CNF) was designed. This catalyst exhibits a half-wave potential of 0.853 V and a Tafel slope of 86.5 mV dec⁻¹ for ORR, as well as an overpotential of 310 mV at 10 mA cm⁻² and a Tafel slope of 57.62 mV dec⁻¹ for OER. Its Δ E value (0.69 V) is lower than that of commercial platinum carbon and ruthenium dioxide (0.75 V), indicating superior bifunctional activity. Electrochemical analysis, X-ray photoelectron spectroscopy, and density functional theory calculations confirm that nanosilver-clusters modulated the electronic structures of cobalt and nicle-iron-layered double hydroxide, optimized their d-band centres, and reduced reaction overpotentials. Use as a ZABs cathode, Ag-NiFe-LDH/Co-CNF delivers an open-circuit voltage of 1.48 V, a peak power density of 152.82 mW cm⁻², and a specific capacity of 796.33 mAh g⁻¹. It also maintains stable performance for over 400 cycles. Additionally, ampere-hour-scale ZABs (4.2 Ah) tested under 0.5 A and 0.5 Ah conditions demonstrate the catalyst's scalability for practical applications.

1. Introduction

Rechargeable zinc-air batteries (ZABs) represent a pivotal energy storage technology, [1–5] due to stable discharge voltage, cost-effectiveness, high energy density and inherent safety. These advantages position ZABs as leading contenders for next-generation sustainable energy solutions. [6–9] Nevertheless, sluggish oxygen electrocatalysis kinetics at air cathodes severely constrain their power density and operational efficiency. Widely used commercial oxygen reduction reactions (ORR) catalysts, such as Pt, and oxygen evolution reactions (OER) catalysts, such as IrO₂ and RuO₂, also face critical challenges, including high cost and limited availability. [10–12] Moreover, these catalysts do not possess the dual functionality beneficial to both ORR and OER, further hindering their scalability for commercial

applications. [13–18] This has been confirmed by many researchers based on studies and development of non-platinum-based metal catalysts. [19–23]

ZIF-8 (zeolitic-imidazolate framework) distinguishes itself within the ZIF family through exceptional structural integrity, tuneable pore architectures, and enhanced charge transport capabilities. These attributes drive their adoption as precursor matrices for engineering diversified functional materials via templated synthesis. [24–26] Han et al. synthesized cobalt nanoparticles, cobalt clusters, and cobalt single atom on nitrogen doped carbon nanoframes by controlling doping agent of cobalt in the imidazole framework of zinc cobalt bimetallic zeolite. The Co single-atom catalyst exhibits high ORR activity in alkaline solution of 0.1 M KOH. [27] Wang et al. systematic investigation effect of Co doping amount and thermal activation temperature on catalytic activity of

E-mail addresses: luokun@cczu.edu.cn (K. Luo), m.edirisinghe@ucl.ac.uk (M. Edirisinghe), g.g.ren@herts.ac.uk (G. Ren).

^{*} Corresponding authors.

zeolite imidazole framework. Co single atom catalyst showed high ORR performance and stability, with half wave unit of 0.8 V vs RHE, and 60 mV lower than commercial catalysts (20 % Pt/C). [28] Cheng et al. constructed a Co nanoparticles/Co single atom catalyst using silica-assisted control of zeolite imidazole framework, further enhancing the mesoporous structure in the catalyst. Co NPs effectively enhanced the ORR catalytic activity of cobalt single atoms, inhibited the formation of hydrogen peroxide, and improved the ORR activity. [29]

Considering that the different mechanisms of ORR and OER require different active sites, an electrocatalyst combination strategy that integrates two or more components can simultaneously meet the dual functional requirements of ORR and OER. [30] Nickel-iron-layered double hydroxide (NiFe LDH) deposited on conductive carbon substrates exhibits excellent OER activity, superior to catalysts under IrO2 alkaline conditions. [31,32] Wang et al. prepared metal N-codoped carbon nano frameworks through controlled pyrolysis of zeolite imidazole frameworks, which have high surface area, excellent conductivity. When combined with NiFe LDH, efficient ORR/OER dual-functional electrocatalysts for ZABs will appear by utilizing their respective ORR/OER high activities. [31] Zhao et al. used atomically dispersed cobalt atoms and NiFe LDH as ORR/OER catalytic site, and integrated them into composite electrocatalysts, exhibiting high ORR/OER performance with a ΔE of 0.63 V, better than commercial catalysts (Pt + $IrO_2 \Delta E = 0.77 \text{ V}$). [33]

Rational heterointerface engineering modulates catalyst electronic configurations, delivering enhanced electrocatalytic functionality through targeted structural design. [34–37] However, transition metals are prone to oxidation, which can lead to catalyst deactivation. [38–43] To address this issue, the introduction of inert metals has proven beneficial. [8,16] These inert metals, characterized by unfilled d-orbitals and moderate adsorption strength, can stabilize the catalyst surface thereby enhance catalytic performance. [44-46] Among them, silver (Ag) nanoparticles have demonstrated excellent catalytic performance for ORR. [47-51] Ag also more cost-effective compared to conventional noble metal catalysts such as Pt, Au, and Pd. [52-54] Building upon these advances, this study introduces a novel nanosilver-enhanced bifunctional catalyst comprising NiFe LDH and Co,N-codoped carbon nanoframes (Ag-NiFe-LDH/Co-CNF). In this design, the catalyst combines synergistic advantages of the silver nanoclusters, NiFe LDH, and carbon nanoframes to optimize the ORR/OER overall performance. The Ag-Co-CNF component synthesized through thermal decomposition of the chemically doped ZIFs, provides a high ORR activity. Here, the NiFe LDH is subsequently deposited onto the carbon nanoframes surrounded with silver nanoclusters that further enhanced OER activity. Additionally, the scalability of the catalyst is evaluated by constructing ampere-hour-scale zinc-air batteries, highlighting its potential for practical applications. This novel catalyst exhibits excellent bifunctional performance, and demonstrates its potential for application in ZABs and other clean energy technologies.

2. Experimental

2.1. Materials and details

Silver nitrate (AgNO₃, 99 %), zinc nitrate hexahydrate (Zn (NO₃)₂·6 H₂O, \geq 98 %), iron(III) nitrate nonahydrate (Fe(NO₃)₃·9 H₂O, \geq 98 %), cobalt nitrate hexahydrate (Co(NO₃)₂·6 H₂O, \geq 98 %), nickel nitrate hexahydrate (Ni(NO₃)₂·6 H₂O, \geq 98 %), zinc acetate (Zn (CH₃COO)₂, \geq 98 %), sodium hydroxide (NaOH, \geq 99 %), 2-methylimidazole (C₄H₆N₂, \geq 98 %), potassium hydroxide (KOH, \geq 99 %), Nafion solution (5 wt%), Pt/C (20 wt% Pt), and IrO₂ (\geq 98 %) were purchased from Shanghai Titan Scientific Co., Ltd. (China). Ethanol (\geq 99.7 %) and N,N-dimethylformamide (DMF, C₃H₇NO, \geq 99 %) were obtained from Sinopharm Chemical Reagent Co., Ltd. (China).

2.2. Synthesis of catalysts

1. Preparation of ZIF-AgCo

A methanol solution (50 mL) of 2-methylimidazole (0.8 mol/L) was placed in a beaker and stirred at 500 rpm using a magnetic stirrer. To this solution, 500 μL of silver nitrate (0.1 mol/L) was added dropwise over a period of 15 min. Subsequently, 50 mL of a methanol solution containing Zn(NO₃)₂·6 H₂O (0.1 mol/L) and Co(NO₃)₂·6 H₂O (0.01 mol/L) was introduced, and the mixture was allowed to react for 3 h, yielding a purple suspension. The product was collected by centrifugation at 12,000 rpm, washed three times with methanol, and freeze-dried to obtain ZIF-AgCo. A control sample, designated as ZIF-Co, was synthesized following the same procedure without the addition of silver nitrate.

2. Preparation of Ag-Co-CNF

ZIF-AgCo was placed in a tube furnace and pyrolyzed under a N_2 atmosphere. The temperature was raised to 900 $^{\circ}C$ at a heating rate of 5 $^{\circ}C/min$ and maintained for 2 h, yielding Ag-Co-CNF. For comparison, Co-CNF was prepared under identical conditions using ZIF-Co as the precursor.

3. Preparation of Ag-NiFe-LDH/Co-CNF

A total of 200 mg of Ag-Co-CNF was dispersed in 20 mL of N,N-dimethylformamide (DMF) containing Ni(NO₃) $_2$ (0.03 mol/L)-6 H₂O and Fe(NO₃) $_3$ 9 H₂O (0.01 mmol). The mixture was subjected to immersion for 24 h, after which the solid was collected via centrifugation and freeze-dried. The resulting powder was then added to 20 mL of NaOH solution (0.1 mol/L) and magnetically stirred for 6 h. The final product, Ag-NiFe-LDH/Co-CNF, was obtained after centrifugation and freeze-drying. For comparison, NiFe-LDH/Co-CNF was synthesized using the same protocol in the absence of silver. A schematic illustration of the synthesis process is provided in Figure S1.

3. Results and discussion

3.1. Structure of the catalysts

The preparation of Ag-NiFe-LDH/Co-CNF is shown in Fig. 1(a). Firstly, ZIF AgCo was characterized by SEM (Figure S2), which show a rhombic dodecahedron morphology and a zeolite imidazole skeleton with good stability, the element mapping is shown in Figure S3, which displays elemental distribution of C, N, Zn, Co, and Ag. After pyrolysis of ZIF AgCo, the SEM images and element mapping of Ag-Co-CNF, as shown in Figure S4, maintained their original morphology and structure, Co and Ag are uniformly distributed on carbon nitrogen matrix. Further TEM characterization (Fig. 1(b-c)) was performed on Ag-Co-CNF. The lattice stripes at 0.204 nm correspond to Co (111) crystal plane, while the lattice stripes at 0.235 nm correspond to Ag (111) crystal plane. Element mapping analysis, as shown in Figure S5, further demonstrates the distribution of cobalt nanoparticles and silver nanoparticles in the catalyst. The close contact of these nanoparticles provides the possibility for Ag to regulate the catalytic activity of Co. ZIF AgCo was characterized by XRD (Figure S6), the XRD curves of ZIF Co and ZIF AgCo are basically consistent, indicating that silver nitrate does not affect the spatial structure gaps of the zeolitic imidazolate framework. And simulated XRD curve of the zeolite imidazole framework. It can be seen that the prepared zeolite imidazole framework is consistent with the calculated XRD. After the pyrolysis of ZIF AgCo, the XRD of Ag-Co-CNF (Figure S7), showed a carbon (002) peak at 26°, corresponding to the PDF card #26-1080 of Carbon. Diffraction peaks appear at 44.4°, corresponding to the Ag (200). As the silver content increases, the peak of silver gradually strengthens. Raman characterization of ZIF AgCo was carried out as shown in Figure S8. The peaks at 176 cm⁻¹, 284 cm⁻¹, and 422 cm⁻¹ can be attributed to vibration of ZnN in the ZnN₄ tetrahedron, the peaks at 266 cm⁻¹ can be attributed to vibration of CoN, the peaks at 686 cm⁻¹ and 694 cm⁻¹ can be attributed to vibration of imidazole ring, the peaks at 836 cm⁻¹, 953 cm⁻¹, and 1024 cm⁻¹ can be attributed to

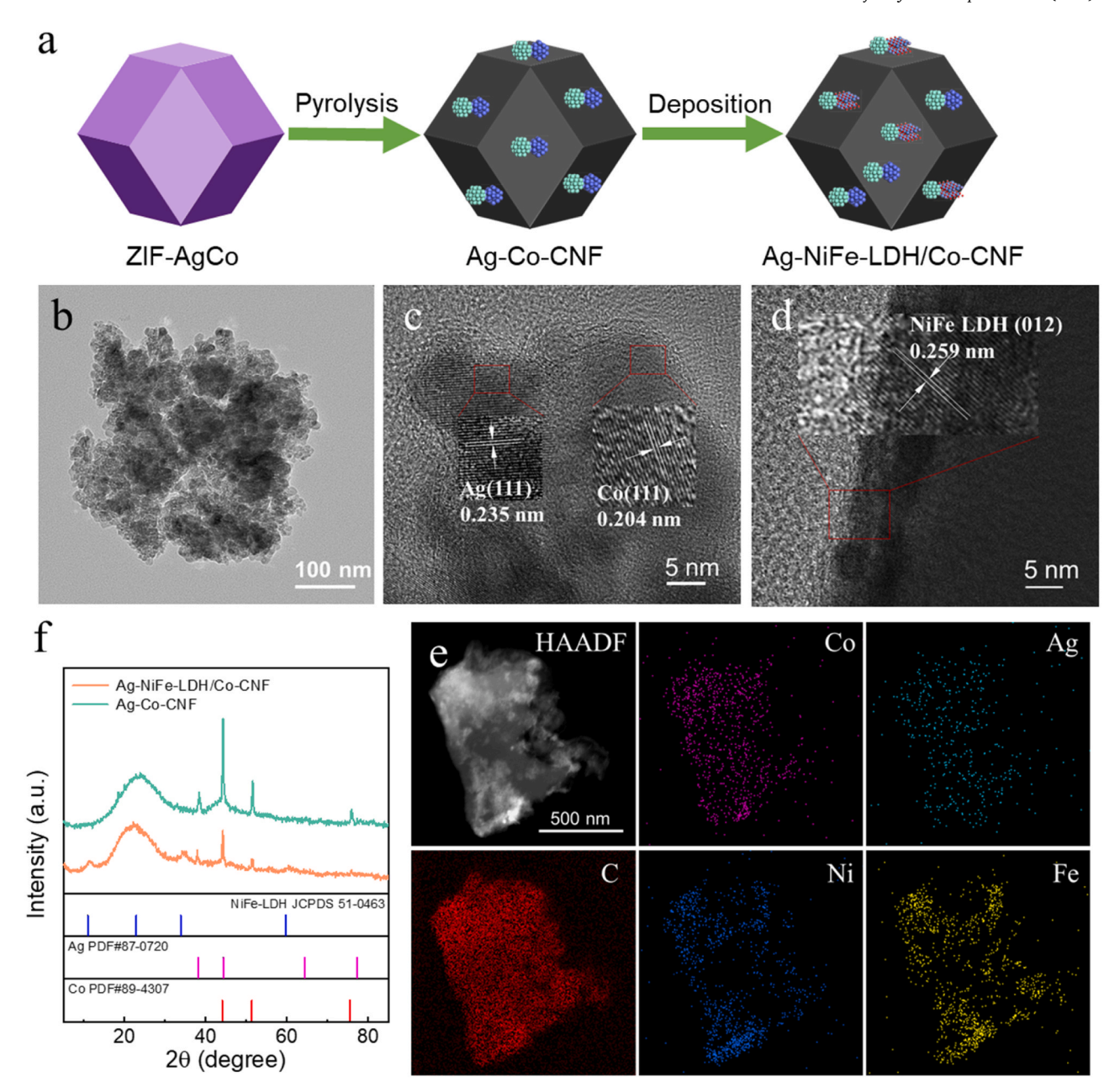


Fig. 1. (a) Schematic diagram of Ag-NiFe-LDH/Co-CNF, (b) TEM image and (c) HRTEM of Ag-Co-CNF, (d) HRTEM of Ag-NiFe-LDH/Co-CNF, (e) High angle annular dark field image (HAADF) image and EDS spectrum of Ag-NiFe-LDH/Co-CNF, (f) XRD of Ag-NiFe-LDH/Co-CNF.

oscillation of C-H in imidazole ring, and stretching vibration of C-N in the imidazole ring can be seen in the $1100{-}1200~{\rm cm}^{-1}$ region. The stretching vibration of C-H in methyl group appears at $1461~{\rm cm}^{-1}$, and the C=C vibration appears at $1500~{\rm cm}^{-1}$. In the high-frequency region, the C-H of methyl and imidazole rings can be observed. Stretching vibrations occur at $2932~{\rm cm}^{-1}$ (methyl ν C-H), $3114~{\rm cm}^{-1}$ and $3134~{\rm cm}^{-1}$ (Imdz ν C-H), respectively. Figure S9 shows the Raman characterization of Ag-Co-CNF. The characteristic D band ($\sim\!1300~{\rm cm}^{-1}$) and G band ($\sim\!1580~{\rm cm}^{-1}$) are observed. The calculated $I_D:I_G$ ratio is approximately 1.1 for all samples, suggesting a comparable level of graphitization and a similar density of defects among the synthesized materials.

NiFe LDH was further prepared on the carbon nano framework of Ag-Co-CNF. The TEM of Ag-NiFe-LDH/Co-CNF is shown in Fig. 1 (d). HRTEM reveals NiFe LDH (012) at 0.259 nm in lattice diffraction. Fig. 1 (e) shows distribution of C, Ag, Co, Ni, and Fe in the EDS spectrum. The XRD of Ag-NiFe-LDH/Co-CNF (Fig. 1(f)), exhibits diffraction peaks at 11°, 23°, 34°, and 60°, corresponding to the (001), (006), (012), and

(110) crystal planes of NiFe LDH (JCPDS 51–0463), which have a structure similar to that of hydrotalcite. Diffraction peaks appear at $38.2^\circ, 44.4^\circ, 64.6^\circ, \text{and}\, 77.59^\circ, \text{corresponding}\, \text{to}\, \text{the}\, \text{Ag}\, (111), \text{Ag}\, (200), \text{Ag}\, (220), \text{and}\, \text{Ag}\, (311)$ crystal planes, corresponding to the PDF card # 87–0720 of Ag. Diffraction peaks appear at $44.23^\circ, 51.53^\circ, \text{and}\, 75.86^\circ, \text{corresponding}\, \text{to}\, \text{the}\, \text{CO}\, (111), \text{CO}\, (200), \text{and}\, \text{CO}\, (220)\, \text{crystal}\, \text{planes}, \text{corresponding}\, \text{to}\, \text{the}\, \text{PDF}\, \text{card}\, \#\, 89–4307\, \text{of}\, \text{Co}.\, \text{Figure}\, \text{S10}\, \text{shows}\, \text{the}\, \text{Raman}\, \text{of}\, \text{Ag-NiFe-LDH/Co-CNF}, \text{with}\, \text{peaks}\, \text{at}\, 477, 546, \text{and}\, 681\, \text{cm}^{-1}\, \text{being}\, \text{characteristic}\, \text{peaks}\, \text{of}\, \text{NiFe}\, \text{LDH}.\, \text{The}\, \text{peak}\, \text{of}\, \text{NiFe}\, \text{LDH}\, \text{in}\, \text{Ag-NiFe-LDH/Co-CNF}\, \text{is}\, \text{more}\, \text{pronounced}\, \text{than}\, \text{that}\, \text{in}\, \text{NiFe-LDH/Co-CNF}, \text{due}\, \text{to}\, \text{the}\, \text{Raman}\, \text{enhancement}\, \text{effect}\, \text{of}\, \text{Ag}.\, \text{This}\, \text{indicates}\, \text{that}\, \text{the}\, \text{defect}\, \text{sites}\, \text{of}\, \text{Ag-Co-CNF}\, \text{adsorb}\, \text{Ni}^{2+}\, \text{and}\, \text{Fe}^{3+}\, \text{cations},\, \text{forming}\, \text{NiFe}\, \text{LDH}\, \text{nanosheet}\, \text{hybrids}.\, \text{Moreover},\, \text{Ag-Co-CNF}\, \text{rich}\, \text{micropores}\, \text{facilitate}\, \text{the}\, \text{growth}\, \text{of}\, \text{NiFe}\, \text{LDH}.$

3.2. Electrocatalytic performance

The effect of Ag addition on the ORR activity of Ag-Co-CNF was studied in 0.1 M KOH saturated with oxygen. Figure S11(a) shows the ORR polarization curves of Ag-Co-CNF at different Ag contents. Figure S11(b) shows the ORR initial potential (Eonset) and half wave potential (E_{1/2)} of Ag-Co-CNF with different Ag contents. The ORR half wave potential values for Ag contents of 0 %, 0.1 %, 0.5 %, 1 %, and 5 % are 0.794 V, 0.810 V, 0.838 V, 0.841 V, and 0.838 V, respectively. As Ag content increases, ORR performance of Ag-Co-CNF first increases and then decreases. The initial potential also shows the same trend, as catalytic performances of Co nanoclusters increases with the increase of Ag content, while the aggregation and growth of nanoparticles with further increase in Ag content actually reduces the catalytic activity. Figure S7 also demonstrates that as Ag content increases, the number of Ag nanoparticles increases and grows. Figure S12-16 compares the polarization curves of Ag-Co-CNF with different Ag contents at different rotational speeds, and fits the K-L equation to calculate number of ORR reaction electrons of the catalyst. The enhancement of Ag-Co-CNF by Ag nanoparticles enhances the 4-electron selectivity of ORR reaction, indicating that its oxygen reduction reaction is dominated by 4electrons. Figure S17 tested the OER polarization curves of Ag-Co-CNF under different Ag contents, and the OER catalytic activity was poor. This indicates that the ORR performance of Ag-NiFe-LDH/Co-CNF catalyst comes from Co nanoparticles, and Ag effectively enhances the catalytic activity of Co nanoparticles.

Fig. 2(a) shows ORR polarization curves of various catalysts at 1600 rpm, and their catalytic performances was evaluated by linear sweep voltammetry (LSV). Among them, the initial potentials (E_{onset}) of Ag-NiFe-LDH/Co-CNF, NiFe-LDH/Co-CNF and 20 % Pt/C are 0.953 V, 0.948 V, and 0.955 V, respectively. The half wave potentials (E_{1/2}) of Ag-NiFe-LDH/Co-CNF, NiFe-LDH/Co-CNF and 20 % Pt/C are 0.853 V, 0.844 V, and 0.862 V (Figure S18). Ag nanoparticles significantly enhance the catalytic performances of NiFe-LDH/Co-CNF, and its performance was similar to that of 20 % Pt/C. The reaction kinetics of the catalyst was studied using the Tafel curve, as shown in Fig. 2(b), The Tafel slopes of Ag-NiFe-LDH/Co-CNF, NiFe-LDH/Co-CNF and 20 % Pt/C are 78.57 mV dec⁻¹, 94.68 mV dec⁻¹, and 86.05 mV dec⁻¹, respectively. This indicates that Ag nanoparticles accelerate the kinetics of oxygen reduction and accelerate the oxygen reduction reaction. The polarization curves of Ag-NiFe-LDH/Co-CNF at different rotational speeds were tested using a rotating disk electrode, as shown in

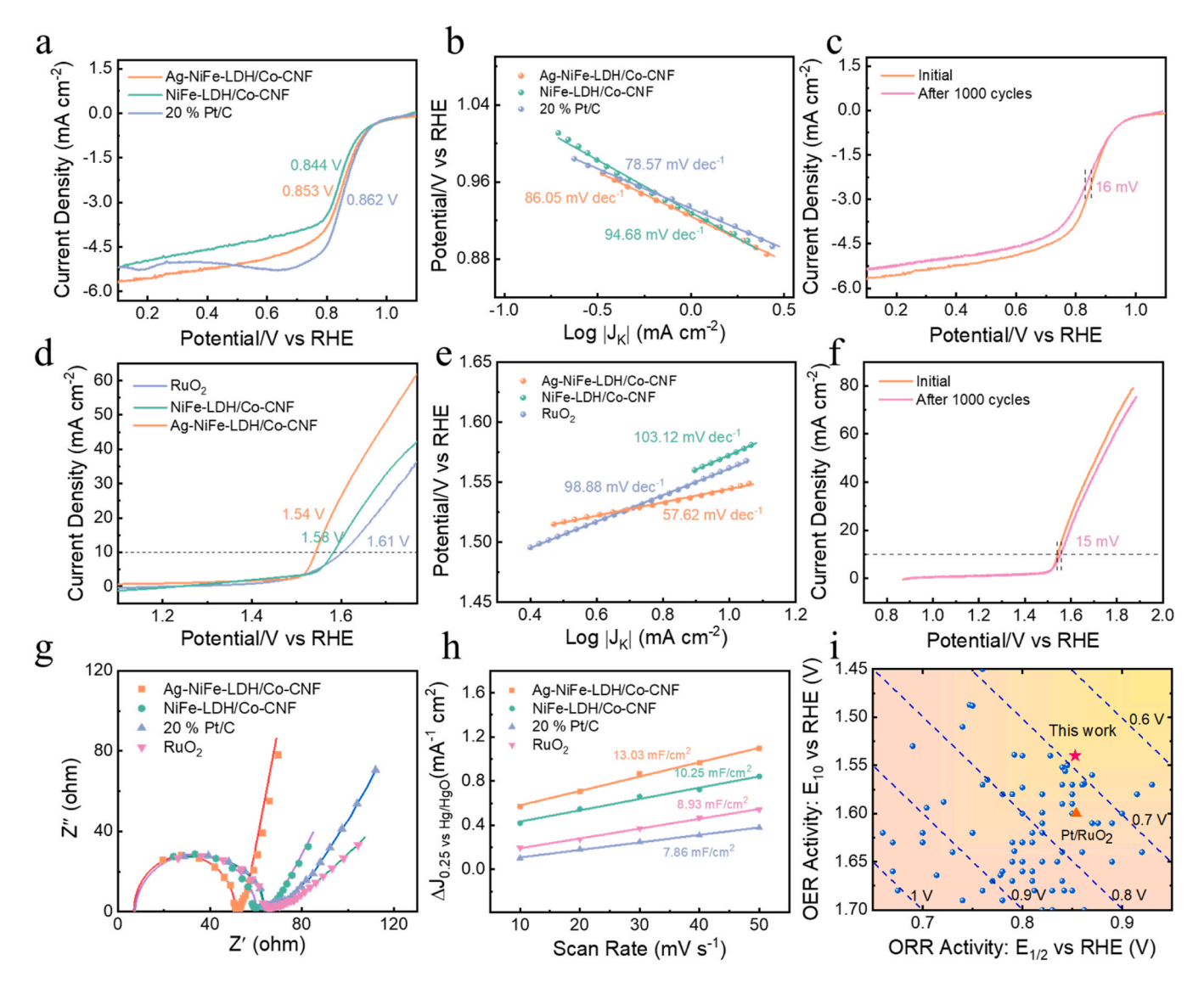


Fig. 2. ORR/OER performances of Ag-NiFe-LDH/Co-CNF. (a) ORR reaction polarization curve, (b) ORR reaction Tafel slope, (c) ORR stability testing, (d) OER reaction polarization curve, (e) OER reaction Tafel slope, (f) OER stability testing, (g) EIS test, (h) ECSA electrochemical active area, (i) bifunctional catalyst performance distribution.

Figure S19. The ORR reaction transfer electron numbers of Ag-NiFe-LDH/Co-CNF and NiFe-LDH/Co-CNF were fitted using the K-L equation, which were 4.0 and 3.8, respectively, indicating that Ag nanoparticles improved the 4-electron selectivity of NiFe-LDH/Co-CNF. The ring current and disk current were tested using a rotating ring disk electrode, as shown in Figure S20(a). The hydrogen peroxide production rate and electron number of the Ag-NiFe-LDH/Co-CNF catalyst were calculated and shown in Figure S20(b). The hydrogen peroxide production rate of Ag-NiFe-LDH/Co-CNF catalyst is close to zero, and the electron transfer number is close to 4, which is consistent with the data of the rotating disk electrode. This result indicates that ORR catalyzed by Ag-NiFe-LDH/Co-CNF follows a four-electron transfer pathway. As shown in Fig. 2(c), after 1000 cycles, the polarization curve shows a half wave potential decay of only 16 mV. Ag-NiFe-LDH/Co-CNF exhibits excellent stability for ORR.

Fig. 2(d) shows the OER polarization curves of various catalysts at 1600 rpm. Among them, potentials of Ag-NiFe-LDH/Co-CNF, NiFe-LDH/Co-CNF and RuO₂ at 10 mA cm⁻² are 1.54 V, 1.56 V, and 1.61 V, respectively, and their overpotentials are 310 mV, 330 mV, and 380 mV, respectively. It can be seen that Ag nanoparticles significantly reduce the OER potential of NiFe-LDH/Co-CNF and enhance the OER catalytic performances. Fig. 2(e) shows the Tafel slopes corresponding to OER polarization curve. The Tafel slopes of Ag-NiFe-LDH/Co-CNF, NiFe-LDH/Co-CNF and RuO₂ are 57.62 mV dec⁻¹, 103.12 mV dec⁻¹, and 98.88 mV dec⁻¹, respectively. This indicates that Ag nanoparticles accelerate the accelerate the OER reaction. As shown in Fig. 2(f), after 1000 cycles, polarization curve shows a potential decay of only 15 mV at a current density of 10 mA cm⁻². Ag-NiFe-LDH/Co-CNF exhibits excellent stability for OER.

We have conducted a series of post-stability analyses to investigate the structural and compositional changes of the Ag-NiFeLDH/Co-CNF catalyst and correlate them with performance degradation. ICP-OES analysis was performed to quantify metal leaching. The initial metal contents were measured as follows: Ag 0.08 %, Co 4.43 %, Fe 3.45 %, and Ni 2.70 %. After stability testing, the values decreased to Ag 0.04 %, Co 1.86 %, Fe 2.33 %, and Ni 1.56 %, indicating significant leaching of active metals, which likely contributes to the observed activity decay. The morphological evolution was examined by SEM and TEM (Figure S21). SEM images show that the overall macro-structure of the catalyst was largely maintained after ORR/OER cycling. However, TEM observations revealed a noticeable reduction in the number of dispersed nanoparticles, suggesting dissolution or detachment of metal clusters during operation. Furthermore, XRD patterns of the cycled catalyst (Figure S22) exhibited weakened diffraction peaks corresponding to Co clusters and the NiFe-LDH phase, supporting the conclusion of structural degradation or loss of crystalline active sites. Collectively, these results indicate that while the carbon framework remains intact, the leaching of metallic species, especially Ag and Co nanoclusters, and the deterioration of the NiFe-LDH phase are major factors underlying the capacity fading and catalytic performance decline.

The AC impedance test is shown in Fig. 2(g), and the fitting results of using Z-view software are shown in Table S1, where R2 is the charge transfer resistance. The fitting values for Ag-NiFe-LDH/Co-CNF, NiFe-LDH/Co-CNF, 20 % Pt/C and RuO2 are 43.2 Ω , 51.98 Ω , 54.46 Ω and 55.34 Ω , respectively. This indicates that Ag nanoparticles regulate electronic structure of NiFe-LDH/Co-CNF, reduce the interfacial resistance, and accelerate the OER process. The above results indicate that Ag nanoclusters enhance the oxygen evolution activity of NiFe-LDH/Co-CNF catalysts. By testing the cyclic voltammetry curves at different scanning speeds as shown in Figure S23 and fitting double-layer capacitance(Fig. 2(h)) of the catalyst. Double-layer capacitance sizes of Ag-NiFe-LDH/Co-CNF, NiFe-LDH/Co-CNF, 20 % Pt/C and RuO2 are 13.03 mF cm⁻², 10.25 mF cm⁻², 8.93 mF cm⁻² and 7.86 mF cm⁻², respectively. The larger specific surface area provides more active sites. To quantitatively evaluate the electrocatalytic activity of bifunctional oxygen electrocatalysts, the total overpotential of ΔE from ORR to OER

was used to indicate bifunctional activity, which was defined as potential difference between the potential (E $_{10}$) of OER and the half wave potential (E $_{1/2}$) of ORR. Based on precious metal based electrocatalysts (such as Pt/C and RuO $_2$), the Δ E is about 0.75 V, while Ag-NiFe-LDH/Co-CNF has good ORR/OER catalytic performances, with a Δ E of about 0.69 V, which is superior to commercial catalysts. Fig. 2(i) compares the catalytic performance of 120 recent ORR/OER bifunctional catalysts, and it can be seen that Ag-NiFe-LDH/Co-CNF has excellent ORR/OER bifunctional catalytic performances compared to existing literature.

3.3. Electronic modulation mechanism

XPS can characterize the surface chemical composition and electronic structure information of samples. The XPS full spectrum of Ag-NiFe-LDH/Co-CNF and NiFe-LDH/Co-CNF is shown in Figure S24. Analysis indicates the presence of cobalt, nitrogen, carbon, oxygen, nickel, iron, and silver in Ag-NiFe-LDH/Co-CNF, with their composition contents as shown in Table S2. The analysis of XPS Ag3d is shown in Figure S25. The peak areas of Ag $3d_{5/2}$ and Ag $3d_{3/2}$ at 367.59 eV and 373.59 eV, respectively. [38,55] This indicates that Ag exists in the form of nanoparticles in the catalyst, indicating the successful preparation of Ag nanoparticles and NiFe LDH heterojunctions, as well as Ag nanoparticles and Co nanoparticles heterojunctions. This heterojunction may be a source of excellent ORR/OER catalysts. The peak fitting results are shown in Table S3. The XPS C1s spectrum is shown in Fig. 3(a), with peaks of C=C, C-C/C-N, C-O/C=O, and N-C-O at 284.4 eV, 284.8 eV, 286.4 eV, and 289.2 eV, respectively. [56] The XPS N1s spectra are shown in Fig. 3(b), with pyridin-N, metal M-N, pyrrole-N, and graphite N at 398.2 eV, 399.1 eV, 399.8 eV, and 400.8 eV, respectively. [56] There is a higher proportion of metal M-N in Ag-NiFe-LDH/Co-CNF, and metal M-N have higher intrinsic activity. [57] The XPS O1s spectrum is shown in Fig. 3(c), with -OH, adsorbed H₂O at 531.2 eV, and 535.5 eV, respectively. [38,56,58] The XPS Co2p spectrum is shown in Fig. 3(d), with $2p_{3/2}$ and $2p_{1/2}$ of zero valent cobalt at 778.1 eV and 792.6 eV, respectively, $2p_{3/2}$ and $2p_{1/2}$ of trivalent cobalt at 780.1 eV and 795.1 eV, respectively, and $2p_{3/2}$ and $2p_{1/2}$ of divalent cobalt at 783.9 eV and 799.6 eV, respectively. The Ag nanoparticles shift the peak position to the left by 0.3 eV, and the proportion of high valence Co atoms increases (Figure S26a). [59,60] The XPS Fe2p spectrum, as shown in Fig. 3(e), shows $2p_{3/2}$ and $2p_{1/2}$ of divalent iron at 709.8 eV and 722.3 eV, and $2p_{3/2}$ and $2p_{1/2}$ of trivalent iron at 712.3 eV and 724.8~eV. Ag nanoparticles shift the peak position by 0.1--0.6~eV to the left, increasing the proportion of high valence Fe atoms (Figure S26b), indicating higher catalytic activity of high valence transition metals. [61] The XPS Ni2p spectrum is shown in Fig. 3(f). There are 2p3/2 and 2p1/2 of divalent nickel at 855.7 eV and 873.3 eV, and the Ag nanoparticles shift the peak position to the left by 0.1 eV. [62] XPS analysis shows that Ag nanoparticles regulate the electronic structure information of NiFe-LDH/Co-CNF, enhancing the catalytic activity.

In order to further analyze catalytic mechanism of Ag-NiFe-LDH/Co-CNF, density functional analysis was used to investigate the reasons for the strengthening of NiFe-LDH/Co-CNF by Ag nanoclusters. Establishing an atomic model as shown in Fig. 4(a), the distribution of d-band orbitals is closely related to ORR/OER catalytic activity. The d-band orbitals of Co sites under influence of Ag nanoparticles were analysed as shown in Fig. 4(b). The d-band centre of Co is -0.574 eV, and under influence of Ag, the d-band centre of Co is -0.688 eV. The centre of the d-band shifts to left by 0.114 eV. The d-band orbitals of Ni and Fe sites under the influence of Ag nanoparticles were analysed as shown in Fig. 4 (c-d). The d-band centre of Fe was -0.681 eV, and under influence of Ag, d-band centre of Fe was -0.677 eV, and the centre of the d-band is shifted to the left by 0.004 eV. The d-band centre of Ni is $-1.307\,$ eV, and under the influence of Ag, d-band centre of Fe is -1.435 eV, and the centre of d-band is shifted to left by 0.128 eV. Calculate the ORR/OER step diagram as shown in Fig. 4(e), and calculation model is provided in Table S4. The calculation results show that Co is the main active site

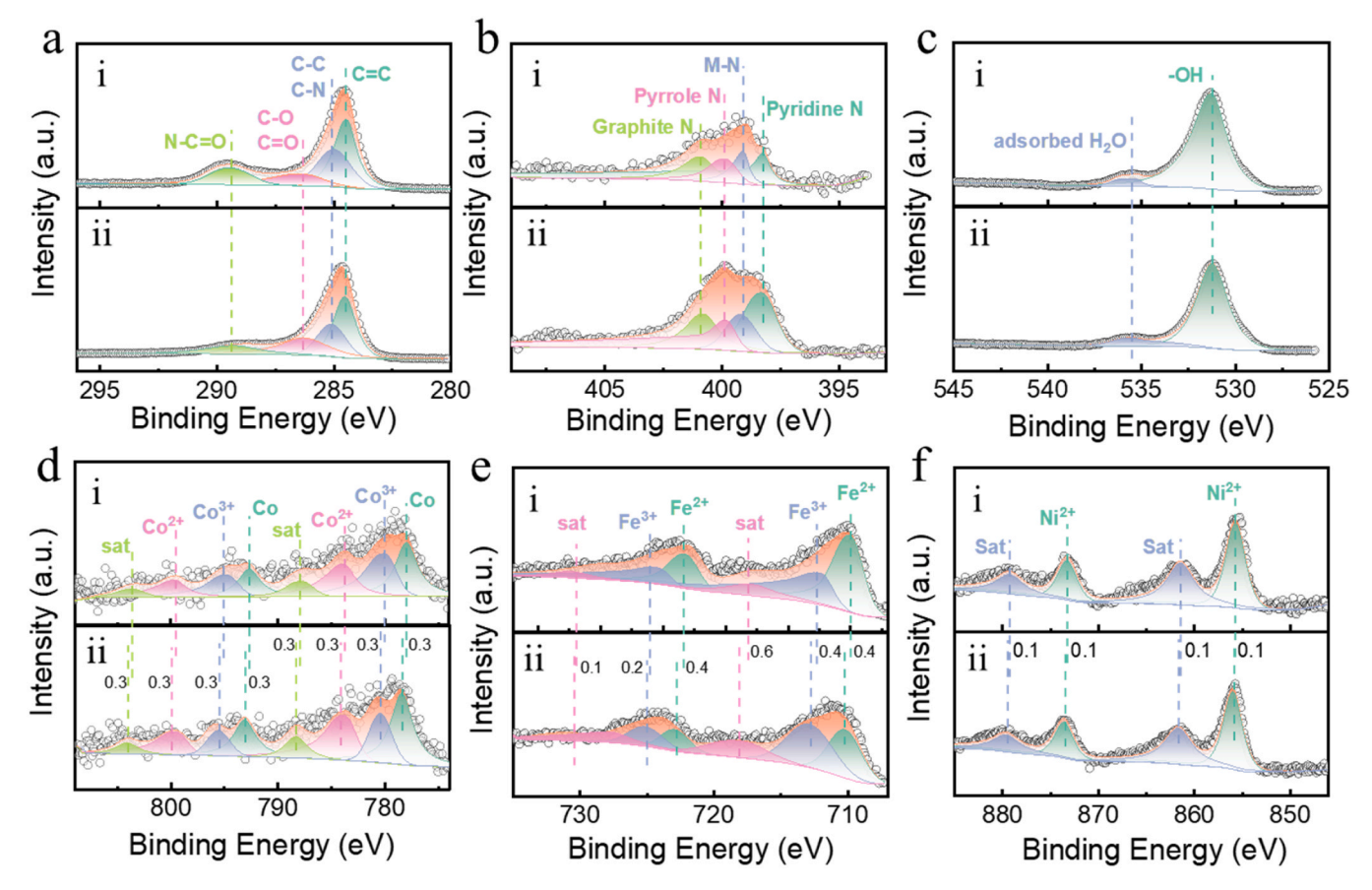


Fig. 3. XPS spectra of (i) NiFe-LDH/Co-CNF and (ii) Ag-NiFe-LDH/Co-CNF. (a) C1s, (b) N1s, (c) O1s, (d) Co2p, (e) Fe2p, (f) Ni2p.

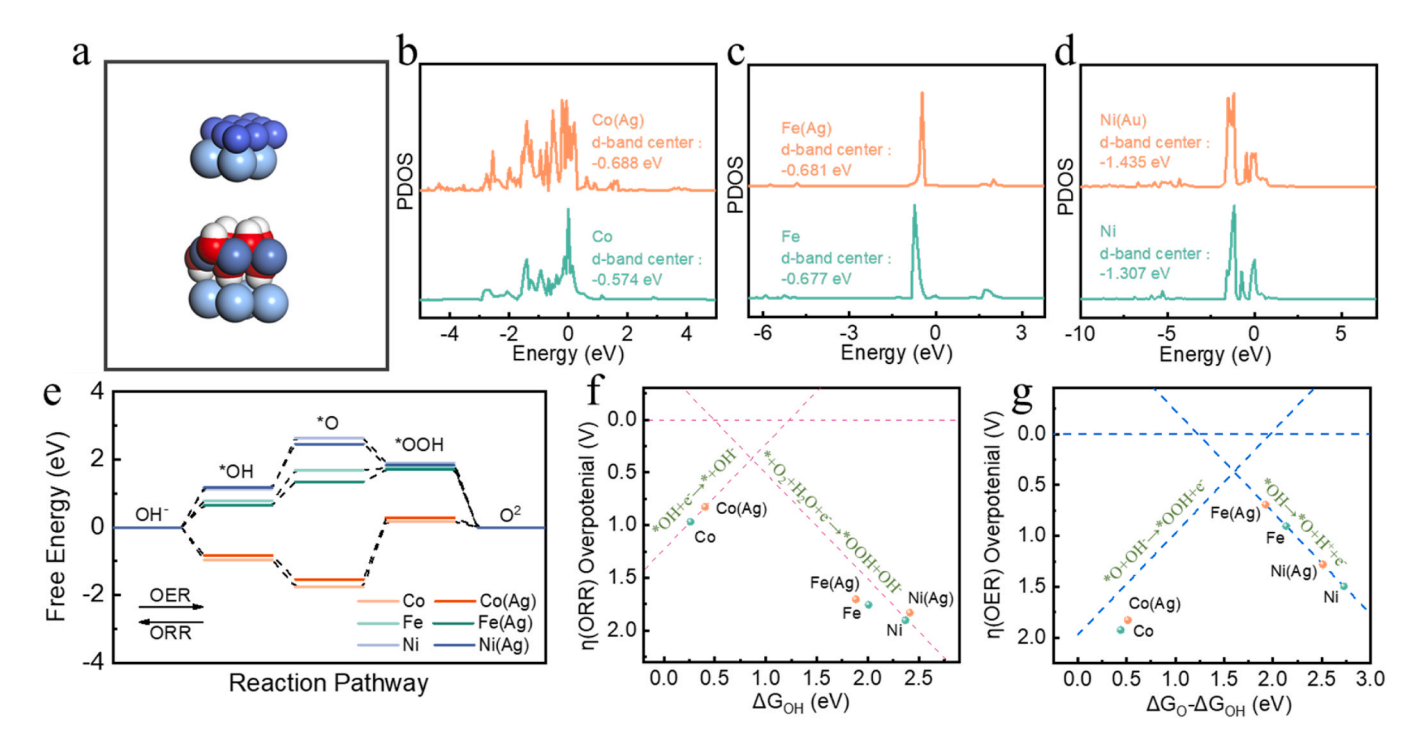


Fig. 4. DFT simulation calculation of catalyst structure and performance. (a) Structural diagrams of Ag nanoparticles and Co nanoparticles, and structural diagrams of Ag nanoparticles and NiFe LDH. (b) The density of states of Co d band orbitals induced and uninduced by Ag nanoparticles. (c) The density of Fe d-band orbital states induced and uninduced by Ag nanoparticles. (d) The density of states of Ni d-band orbitals induced and uninduced by Ag nanoparticles. (e) The step plot curve of each metal active site. (f) ORR volcano map. (g) OER volcano map.

centre of ORR, and under Ag regulation, the overpotential of ORR decreased from 0.968 eV to 0.825 eV. The overpotential of Fe as the main active site centre in OER decreased from 0.904 eV to 0.693 eV (Table S5), which is consistent with the results in the literature. [28,63] According to the proportional relationship, the ORR active volcano diagram is described using ΔG_{OH} as shown in Fig. 4(f), and the OER active volcano diagram is described using ΔG_{*O} - ΔG_{*OH} as shown in Fig. 4(g). Both OER and ORR activities can be divided into strong adsorption zones and weak adsorption zones. For ORR reaction step 1 (*+O₂ \rightarrow *OOH) and step 4 (*OH \rightarrow *+H₂O), are the main rate limiting steps, while for OER reaction steps 2 (*OH \rightarrow *O) and step 3 (*O \rightarrow *OOH), are main rate limiting steps. The calculation results show that Ag effectively enhances the ORR/OER dual functional activity of NiFe-LDH/Co-CNF. This enhancement mainly comes from modulation of electronic structure, and the development of high catalytic activity multifunctional catalysts can be achieved through reasonable structural design.

While ex-situ XPS and DFT calculations strongly support the electronic modulation effect of Ag clusters, future studies employing in situ techniques, such as X-ray absorption spectroscopy XAS (synchrotron X-ray absorption spectroscopy), XPS or Raman under operating conditions, would be highly valuable to directly capture the dynamic evolution of the active sites' valence states and local coordination environments during electrocatalysis.

3.4. Zinc-air batteries performances

Further preparation of the positive electrode of ZABs using air cathode catalyst was carried out, and the performance of ZABs was studied. The open circuit potentials (Fig. 5(a)) of Ag-NiFe-LDH/Co-CNF, NiFe-LDH/Co-CNF and 20 % Pt/C+RuO₂ batteries are 1.48 V, 1.45 V, and 1.45 V, respectively. The ZABs assembled with Ag-NiFe-LDH/Co-CNF has a higher open circuit potential. The full discharge analysis of ZABs with Ag-NiFe-LDH/Co-CNF, NiFe-LDH/Co-CNF and 20 % Pt/C+RuO₂ catalysts is shown in Fig. 5 (d), with discharge specific capacities of 796.3 mAh $g_{\rm Zn}^{-1}$, 755.5 mAh $g_{\rm Zn}^{-1}$, and 694.3 mAh $g_{\rm Zn}^{-1}$

respectively. Ag-NiFe-LDH/Co-CNF has a higher discharge capacity. Fig. 5(c) shows the curves of different discharge current densities, and the discharge voltage decreases with increasing current density. The catalytic activity of Ag-NiFe-LDH/Co-CNF is better than that of NiFe-LDH/Co-CNF and 20 % Pt/C+RuO₂. The ORR polarization curve and discharge power density of ZABs are shown in Fig. 5(d), indicating that Ag-NiFe-LDH/Co-CNF have highest discharge power density of 152.8 mW cm⁻². while power density of 20 % Pt/C+RuO₂ was only 102.4 mW cm⁻². This is due to excellent ORR/OER dual functional performances of Ag-NiFe-LDH/Co-CNF. The cycle performance test of ZABs is shown in Fig. 5 (e). It can be seen that during 400 cycles of ZABs, the charge discharge potential difference of Ag-NiFe-LDH/Co-CNF is smaller than that of NiFe-LDH/Co-CNF and 20 % Pt/C+RuO₂. This indicates that Ag-NiFe-LDH/Co-CNF also exhibits excellent bifunctional activity in ZABs.

To investigate the practicality of rechargeable ZABs, we constructed a battery with an ampere hour scale (Fig. 6a). The external dimensions of each ZABs are $13.0 \times 13.0 \times 4.3 \, \mathrm{cm}^3$, and the area electrocatalyst mass loading is 1 mg cm $^{-2}$. The constant current discharge performance of ZABs with ampere hour scale was tested, and they were discharged for 8.4 h at an input current of 0.5 A, with a capacity of 4.2 Ah, which may support long-term energy storage (Fig. 6b). The average voltages were 1.29 V, 1.21 V, 1.14 V, and 0.99 V at output currents of 0.10, 0.50, 1.0, and 2.0 A, respectively (Fig. 6c). In addition, cyclic tests were conducted under actual conditions of 0.5 A and 0.5 Ah to explore the durability of ZABs (Fig. 6d)., They maintained initial discharge and charging voltages of 1.0 and 2.2 V after cycles, indicating their potential to solve energy storage problems for various renewable resources.

Overall, the implementation of battery powered platforms in manufacturing and energy storage is highlighting the global focus on sustainable, high performance electrochemical systems. In this context, the batteries proposed in this study show clear promise for real world usage, in parallel with the battery powered applications on a global scale for off grid manufacturing, which further underscores this shift toward cleaner, modular technologies and complements sustainable production

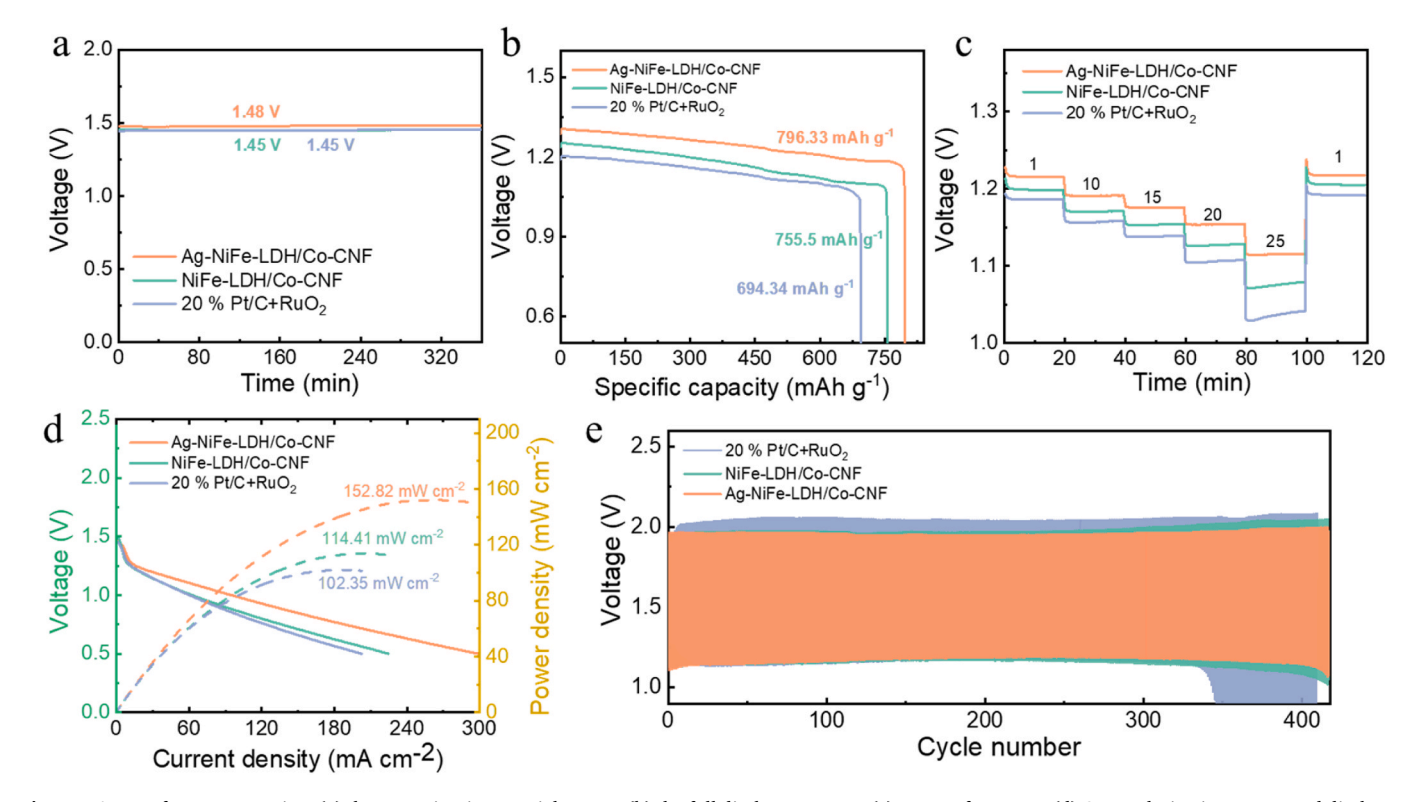


Fig. 5. ZABs performances testing, (a) the open circuit potential curves, (b) the full discharge curves, (c) rate performance, (d) ORR polarization curves and discharge power density curves, (e) the cycle curves.

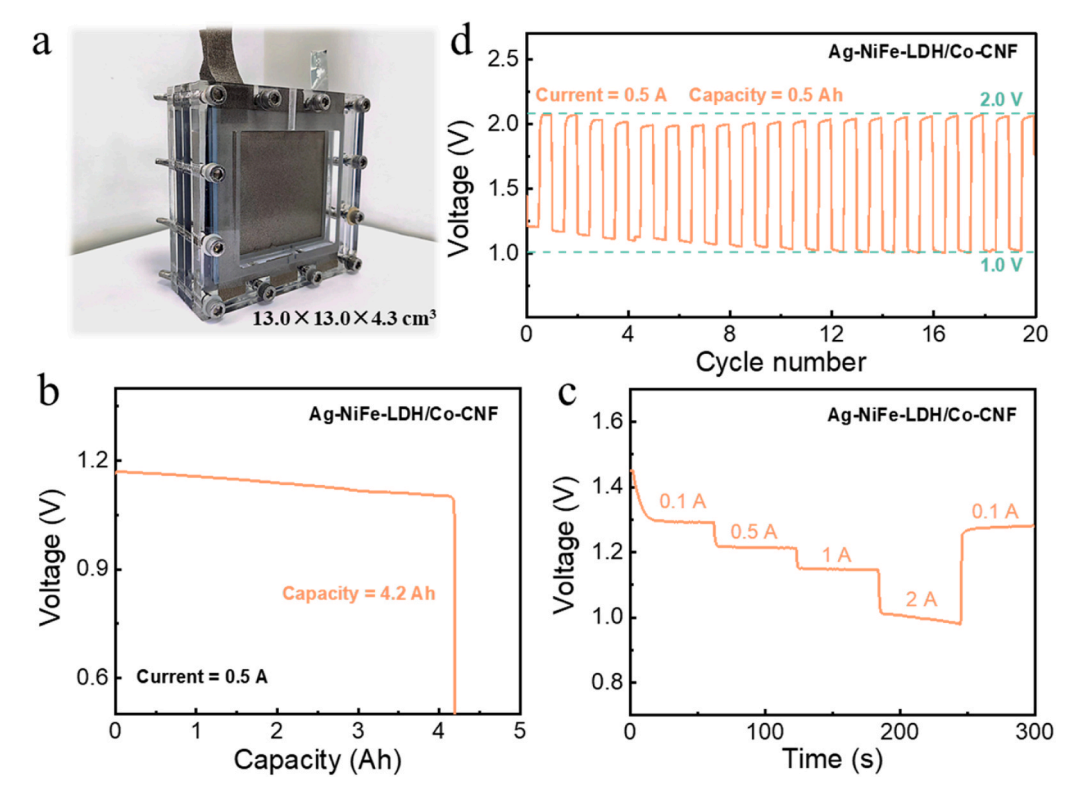


Fig. 6. Ampere-hour-scale ZABs performances testing. (a) optical photograph, (b) full discharge performance, (c) rate performances at different current densities, (d) galvanostatic cycle curves of ZABs.

methodologies. [64]

4. Conclusions

In summary, we successfully developed a nanoscale heterogeneous ORR/OER bifunctional catalyst, Ag-NiFe-LDH/Co-CNF, by harnessing electron modulation effects of Ag nanoclusters. This catalyst leveraged the electron modulation effect of Ag nanoclusters to optimize electronic structure of NiFe LDH, thereby enhancing its oxygen evolution reaction (OER) performance. Simultaneously, it modulates oxygen reduction reaction (ORR) performance of Co nanocrystals, significantly improving the overall ORR performance. The catalyst achieves a half-wave potential of 0.85 V for ORR, while exhibiting an OER overpotential of 310 mV at 10 mA cm⁻². Notably, its ΔE value (0.69 V) is lower than that of commercial catalysts (0.75 V), validating exceptional bifunctional activity. When integrated into ZABs, the battery exhibits high peak power and energy density. Ampere-hour-scale ZABs with a capacity of 4.2 Ah were assembled and tested under 0.5 A and 0.5 Ah cycle conditions, underscoring their practical application potential. Furthermore, the simple synthesis process and cost-effective design indicate its potential for scalable production and broader application in emerging energy conversion and storage devices.

CRediT authorship contribution statement

Zhihong Luo: Methodology, Conceptualization. Yaming Pang: Software, Conceptualization. Degui Li: Software, Resources. Xiangqun Zhuge: Methodology, Investigation. Kun Luo: Writing – review & editing, Software, Resources. Yurong Ren: Resources. Mehmet Onur Aydogdu: Writing – review & editing. Tong Liu: Writing – original draft, Methodology, Investigation, Formal analysis, Data curation, Conceptualization. Mohan Edirisinghe: Writing – review & editing, Conceptualization. Guogang Ren: Writing – review & editing, Resources, Methodology, Conceptualization.

Declaration of Competing Interest

The authors declare that they have no known competing financial interests or personal relationships that could have appeared to influence the work reported in this paper.

Acknowledgement

This work was supported by the National Natural Science Foundation of China (No. 52474431), and the award from the UK Royal Society (IEC \NSFC\201155).

Appendix A. Supporting information

Supplementary data associated with this article can be found in the online version at doi:10.1016/j.jallcom.2025.184255.

References

- [1] H. Chen, E. Lv, M. Qin, X. Qu, H. Yu, X. Zhang, X. Dong, Mott-Schottky heterojunction design in Cu/Fe₂N@NC catalyst with interfacial electron redistribution for enhanced oxygen reduction reaction in zinc-air batteries, J. Alloy. Compd. 1032 (2025) 181134, https://doi.org/10.1016/j. jallcom.2025.181134.
- [2] Q.-h Li, Y. Liu, P. Guo, Q.-h Cai, J.-j Zhang, L. Zhao, Z.-b Wang, Platinum nanoparticles anchored on Ru-N_X doped carbon: synergistic dual-active site catalysts for oxygen reduction reactions, J. Alloy. Compd. 1010 (2025) 178150, https://doi.org/10.1016/j.jallcom.2024.178150.
- [3] Z. Zhang, J. Liu, F. Liu, O. Ruzimuradov, H. Yang, D. Fang, Pre-lithiation depositing PtCu nanoparticles onto N-doped carbon as an efficient catalyst for oxygen reduction reaction, J. Alloy. Compd. 1036 (2025) 182057, https://doi.org/ 10.1016/j.jallcom.2025.182057.
- [4] D. Bhalothia, A. Beniwal, Y.-W. Wu, A. Hu, A. Bagaria, T.-Y. Chen, Surface-decorated Sn-oxide and atomic Sn-metal clusters boost the oxygen reduction reaction performance of palladium nanoparticles, J. Alloy. Compd. 1014 (2025) 178583, https://doi.org/10.1016/j.jallcom.2025.178583.
- [5] R. Dang, H. Liang, F. Huang, F. Yin, Controllable gas-phase synthesis of Pt-Gd nanoalloy catalysts and electrocatalytic performance for oxygen reduction

- reaction, J. Alloy. Compd. 1021 (2025) 179748, https://doi.org/10.1016/j.
- [6] J. Dong, Y. Pang, D. Bildan, L. Xing, X. Liu, X. Zhuge, Z. Yuan, Y. Ren, D. Liu, W. Lei, K. Luo, Fe₃Co nanoparticles embedded carbon nanotube complex as effective bifunctional electrocatalysts for rechargeable zinc-air batteries, Chem. Eng. J. 500 (2024) 157309, https://doi.org/10.1016/j.cej.2024.157309.
- [7] Z. Luo, M. Zhou, J. Lu, T. Xu, X. Zhuge, X. Zhong, L. Liu, Y. Li, K. Luo, X. Li, W. lei, D. Liu, 3D fluorinated honeycomb cavity morphology through modulated crystal facet for dendrite-free aqueous zinc batteries, Chem. Eng. J. 506 (2025) 159909, https://doi.org/10.1016/j.cej.2025.159909.
- [8] T. Liu, J. Lu, Z. Chen, Z. Luo, Y. Ren, X. Zhuge, K. Luo, G. Ren, W. Lei, D. Liu, Advances, mechanisms and applications in oxygen evolution electrocatalysis of gold-driven, Chem. Eng. J. 496 (2024) 153719, https://doi.org/10.1016/j. cei.2024.153719.
- [9] H. Mu, K. Luo, Y. Pang, X. Zhuge, Z. Ding, Y. Ren, D. Li, Z. Luo, B.B. Xu, M. Bayati, X. Liu, Mesoporous SiO₂ anode armour for lithium oxygen battery, Chem. Eng. J. 475 (2023), https://doi.org/10.1016/j.cej.2023.146489.
- [10] X.W. Lv, Z. Wang, Z. Lai, Y. Liu, T. Ma, J. Geng, Z.Y. Yuan, Rechargeable Zinc–Air batteries: advances, challenges, and prospects, Small (2023) 2306396, https://doi. org/10.1002/smll.202306396.
- [11] H. Mu, X. Zhuge, G. Ren, K. Luo, Z. Ding, Y. Ren, Z. Luo, M. Bayati, B.B. Xu, X. Liu, Dual functional mesoporous silica colloidal electrolyte for lithium-oxygen batteries, Chem. Eng. J. 455 (2023) 140761, https://doi.org/10.1016/j. cei 2022 140761
- [12] Y. Liu, D. Bildan, X. Zhuge, T. Liu, H. Zhong, Z. Luo, H. Lei, K. Luo, Y. Ren, M. Bayati, X. Liu, Composite gel polymer electrolyte for high-performance flexible Zinc-Air batteries, Small (2024) 2408015, https://doi.org/10.1002/ cmll.202408015
- [13] J. Fu, Z.P. Cano, M.G. Park, A. Yu, M. Fowler, Z. Chen, Electrically rechargeable Zinc-Air batteries: progress, challenges, and perspectives, Adv. Mater. 29 (7) (2017) 1604685, https://doi.org/10.1002/adma.201604685.
- [14] X. Chen, Z. Zhou, H.E. Karahan, Q. Shao, L. Wei, Y. Chen, Recent advances in materials and design of electrochemically rechargeable zinc-air batteries, Small 14 (44) (2018) 1801929, https://doi.org/10.1002/smll.201801929.
- [15] Y. Liu, X. Zhuge, T. Liu, Z. Luo, K. Luo, Y. Li, Y. Ren, M. Bayati, X. Liu, Cold-plasma activation converting conductive agent in spent Li-ion batteries to bifunctional oxygen reduction/evolution electrocatalyst for zinc-air batteries, J. Colloid Interface Sci. 665 (2024) 793–800, https://doi.org/10.1016/j.jcis.2024.03.169.
- [16] J. Zhang, X. Zhuge, T. Liu, K. Luo, J. Lyu, Y. Ren, Y. Li, L. Xing, Copper-doped nickel oxide supported on carbon black for highly active oxygen reduction/ evolution electrocatalysis, Mater. Today Commun. 38 (2024) 108335, https://doi. org/10.1016/j.mtcomm.2024.108335.
- [17] K. Luo, Y. Li, T. Liu, X. Zhuge, E. Chung, A.R. Timms, S.P. Graham, G. Ren, Functionalized copper nanoparticles with gold nanoclusters: part I. Highly selective electrosynthesis of hydrogen peroxide, ACS Omega 8 (39) (2023) 36171–36178. https://doi.org/10.1021/acsomega.3c03665.
- [18] K. Luo, M. Zhou, T. Liu, X. Zhuge, T.X. Liu, M. Bayati, Y. Ren, Z. Luo, A high-performance Zinc-Air battery cathode catalyst from recycling of spent lithium iron phosphate batteries, Small Struct. 4 (11) (2023) 2300107, https://doi.org/10.1002/sstr.202300107.
- [19] Y. Feng, Y. Xie, Y. Yu, Y. Chen, Q. Liu, H. Bao, F. Luo, S. Pan, Z. Yang, Electronic metal-support interaction induces hydrogen spillover and platinum utilization in hydrogen evolution reaction, Angew. Chem. Int. Ed. 64 (1) (2025) e202413417, https://doi.org/10.1002/anie.202413417.
- [20] Q. Li, Y. Feng, Y. Yu, Y. Chen, Y. Xie, F. Luo, Z. Yang, Engineering eg filling of RuO₂ enables a robust and stable acidic water oxidation, Chin. Chem. Lett. 36 (3) (2025) 110612, https://doi.org/10.1016/j.cclet.2024.110612.
- [21] Y. Yan, B. Wang, C. Li, F. Luo, Y. Li, Y. Xie, Q. Zhang, Z. Yang, A systematic investigation on the advantage of confinement effect by nitrogen doped carbon nanotubes for hydrogen evolution reaction, J. Colloid Interface Sci. 693 (2025) 137667, https://doi.org/10.1016/j.jcis.2025.137667.
 [22] Q. Li, Y. Feng, Y. Xie, Q. Xu, Y. Li, Y. Yu, F. Luo, Z. Yang, MOF derived RuO₂/V₂O₅
- [22] Q. Li, Y. Feng, Y. Xie, Q. Xu, Y. Li, Y. Yu, F. Luo, Z. Yang, MOF derived RuO₂/V₂O₅ nanoneedles for robust and stable water oxidation in acid, Chin. Chem. Lett. 36 (7) (2025) 111074, https://doi.org/10.1016/j.cclet.2025.111074.
- [23] Y. Xie, Y. Feng, S. Zhu, Y. Yu, H. Bao, Q. Liu, F. Luo, Z. Yang, Modulation in spin state of Co₃O₄ decorated fe single atom enables a superior rechargeable Zinc-Air battery performance, Adv. Mater. 37 (5) (2025) 2414801, https://doi.org/ 10.1002/adma.202414801.
- [24] S.Q. Shen, Y.Y. Sun, H. Sun, Y.P. Pang, S.X. Xia, T.Q. Chen, S.Y. Zheng, T. Yuan, Research progress in ZIF-8 derived single atomic catalysts for oxygen reduction reaction, Catalysts 12 (5) (2022), https://doi.org/10.3390/catal12050525.
- [25] N.Y. Cheng, L. Ren, X. Xu, Y. Du, S.X. Dou, Recent development of zeolitic imidazolate frameworks (ZIFs) derived porous carbon based materials as electrocatalysts, Adv. Energy Mater. 8 (25) (2018) 21, https://doi.org/10.1002/ aenm.201801257.
- [26] X. Li, H. Liang, X. Liu, Y. Zhang, Z. Liu, H. Fan, Zeolite imidazolate frameworks (ZIFs) derived nanomaterials and their hybrids for advanced secondary batteries and electrocatalysis, Chem. Rec. (2022) e202200105, https://doi.org/10.1002/ ter.202200105
- [27] X. Han, X. Ling, Y. Wang, T. Ma, C. Zhong, W. Hu, Y. Deng, Generation of nanoparticle, atomic-cluster, and single-atom cobalt catalysts from zeolitic imidazole frameworks by spatial isolation and their use in zinc-air batteries, Angew. Chem. Int Ed. Engl. 58 (16) (2019) 5359–5364, https://doi.org/10.1002/ price.201001100
- [28] X.X. Wang, D.A. Cullen, Y.-T. Pan, S. Hwang, M. Wang, Z. Feng, J. Wang, M. H. Engelhard, H. Zhang, Y. He, Y. Shao, D. Su, K.L. More, J.S. Spendelow, G. Wu,

- Nitrogen-Coordinated single cobalt atom catalysts for oxygen reduction in proton exchange membrane fuel cells, Adv. Mater. 30 (11) (2018) 1706758, https://doi.org/10.1002/adma.201706758.
- [29] X. Cheng, J. Yang, W. Yan, Y. Han, X. Qu, S. Yin, C. Chen, R. Ji, Y. Li, G. Li, G. Li, Y. Jiang, S. Sun, Nano-geometric deformation and synergistic conanoparticles—Co-N₄ composite sites for proton exchange membrane fuel cells, Energy Environ. Sci. 14 (11) (2021) 5958–5967, https://doi.org/10.1039/dlag01715b
- [30] S. Bhattacharyya, C. Das, T.K. Maji, MOF derived carbon based nanocomposite materials as efficient electrocatalysts for oxygen reduction and oxygen and hydrogen evolution reactions, RSC Adv. 8 (47) (2018) 26728–26754, https://doi. org/10.1039/c8ra05102i.
- [31] Q. Wang, L. Shang, R. Shi, X. Zhang, Y. Zhao, G.I.N. Waterhouse, L.Z. Wu, C. H. Tung, T. Zhang, NiFe layered double hydroxide nanoparticles on Co,N-Codoped carbon nanoframes as efficient bifunctional catalysts for rechargeable Zinc-Air batteries, Adv. Energy Mater. 7 (21) (2017) 1700467, https://doi.org/10.1002/aepm 201700467
- [32] L. Li, X. Tang, B. Wu, B. Huang, K. Yuan, Y. Chen, Advanced architectures of air electrodes in Zinc–Air batteries and hydrogen fuel cells, Adv. Mater. (2024) 2308326, https://doi.org/10.1002/adma.202308326.
- [33] C.X. Zhao, J.N. Liu, J. Wang, D. Ren, J. Yu, X. Chen, B.Q. Li, Q. Zhang, A $\Delta E=0.63$ v bifunctional oxygen electrocatalyst enables High-Rate and Long-Cycling Zinc-Air batteries, Adv. Mater. 33 (15) (2021) 2008606, https://doi.org/10.1002/adma.202008606.
- [34] J. Balamurugan, P.M. Austeria, J.B. Kim, E.-S. Jeong, H.-H. Huang, D.H. Kim, N. Koratkar, S.O. Kim, Electrocatalysts for zinc–air batteries featuring single molybdenum atoms in a nitrogen-doped carbon framework, Adv. Mater. 35 (35) (2023) 2302625, https://doi.org/10.1002/adma.202302625.
- [35] J. Balamurugan, T.T. Nguyen, D.H. Kim, N.H. Kim, J.H. Lee, 3D nickel molybdenum oxyselenide (Ni_{1-x}Mo_xOSe) nanoarchitectures as advanced multifunctional catalyst for Zn-air batteries and water splitting, Appl. Catal. B Environ. 286 (2021) 119909, https://doi.org/10.1016/j.apcatb.2021.119909.
- [36] J. Balamurugan, T.T. Nguyen, N.H. Kim, D.H. Kim, J.H. Lee, Novel core-shell CuMo-oxynitride@N-doped graphene nanohybrid as multifunctional catalysts for rechargeable zinc-air batteries and water splitting, Nano Energy 85 (2021) 105987, https://doi.org/10.1016/j.nanoen.2021.105987.
- [37] G. Bharath, C. Liu, F. Banat, A. Kumar, A. Hai, A. Kumar Nadda, V. Kumar Gupta, M. Abu Haija, J. Balamurugan, Plasmonic au nanoparticles anchored 2D WS₂@ RGO for high-performance photoelectrochemical nitrogen reduction to ammonia, Chem. Eng. J. 465 (2023) 143040, https://doi.org/10.1016/j.cej.2023.143040.
- [38] X.C. Wang, Z.H. Zang, C.Y. Fan, Y.T. Zhang, X. Li, L.L. Li, X.F. Yu, X.J. Yang, Z. M. Lu, X.H. Zhang, Effects of group IB metals of Au/Ag/Cu on boosting oxygen evolution reaction of cobalt hydroxide, ChemCatChem 15 (7) (2023) 202300033, https://doi.org/10.1002/cctc.202300033.
- [39] Z.H. Luo, F.J. Li, C.L. Hu, L.K. Yin, D.G. Li, C.H. Ji, X.Q. Zhuge, K. Zhang, K. Luo, Highly dispersed silver nanoparticles for performance-enhanced lithium oxygen batteries, J. Mater. Sci. Technol. 73 (2021) 171–177, https://doi.org/10.1016/j. imst 2020 07 039
- [40] D.G. Li, Y.J. Luo, J.X. Lan, Z.H. Luo, F.J. Li, K. Luo, Synthesis of amphiphilic janus gold nanoparticles stabilized with triphenylphosphine and D-penicillamine by ligand exchange at toluene/water emulsion interface, Gold. Bull. 53 (2) (2020) 55–62, https://doi.org/10.1007/s13404-020-00274-1.
- [41] Y. Wang, Y.C. Lu, Nonaqueous Lithium-Oxygen batteries: reaction mechanism and critical open questions, Energy Storage Mater. 28 (2020) 235–246, https://doi.org/ 10.1016/j.ensm.2020.03.007.
- [42] W. Chen, Z. Luo, X. Zhuge, Z. Ding, Y. Ren, A. Loya, Y. Li, K. Luo, Protecting lithium anode with ionic liquid modified poly(vinylidene fluoride) single ion conducting separators for iodide-assisted lithium oxygen batteries, J. Energy Storage 50 (2022) 104580, https://doi.org/10.1016/j.est.2022.104580.
- [43] J. Fang, Z. Ding, Y. Ling, J. Li, X. Zhuge, Z. Luo, Y. Ren, K. Luo, Green recycling and regeneration of $LiNi_{0.5}Co_{0.2}Mn_{0.3}O_2$ from spent Lithium-ion batteries assisted by sodium sulfate electrolysis, Chem. Eng. J. 440 (2022) 135880, https://doi.org/10.1016/j.cej.2022.135880.
- [44] F.W.T. Goh, Z.L. Liu, X.M. Ge, Y. Zong, G.J. Du, T.S.A. Hor, Ag nanoparticle-modified MnO₂ nanorods catalyst for use as an air electrode in zinc-air battery, Electrochim. Acta 114 (2013) 598–604, https://doi.org/10.1016/j.electacta.2013.10.116.
- [45] T. Li, Z.L. He, X. Liu, M. Jiang, Q. Liao, R.D. Ding, S. Liu, C. Zhao, W.B. Guo, S. S. Zhang, H. He, Interface interaction of Ag-CeO₂-Co₃O₄ facilitate ORR/OER activity for Zn-air battery, Surf. Interfaces 33 (2022) 102270, https://doi.org/10.1016/j.surfin.2022.102270.
- [46] Q. Wang, H. Miao, S.S. Sun, Y.J. Xue, Z.P. Liu, One-Pot synthesis of Co₃O₄/Ag nanoparticles supported on N-Doped graphene as efficient bifunctional oxygen catalysts for flexible rechargeable Zinc-Air batteries. Chemistry, A Eur. J. 24 (55) (2018) 14816–14823, https://doi.org/10.1002/chem.201803236.
- [47] B. Hvolbæk, T.V.W. Janssens, B.S. Clausen, H. Falsig, C.H. Christensen, J. K. Nørskov, Catalytic activity of au nanoparticles, Nano Today 2 (4) (2007) 14–18, https://doi.org/10.1016/S1748-0132(07)70113-5.
- [48] K. Luo, H. Wang, X. Li, Electrocatalytic activity of ligand-protected gold particles: formaldehyde oxidation, Gold. Bull. 47 (1-2) (2013) 41–46, https://doi.org/ 10.1007/s13404-013-0110-0.
- [49] D. Li, T. Liu, Y. Luo, X. Zhuge, K. Luo, Z. Luo, X. Liu, K. Zhang, Reversible ligand exchange of triphenylphosphine with thiols on gold nanoparticles for janus modification and catalyst recycling, Sep. Purif. Technol. 322 (2023) 124154, https://doi.org/10.1016/j.seppur.2023.124154.

- [50] Y.S. Zhang, L.K. Yin, Z.H. Luo, X.Q. Zhuge, P. Wei, Z. Song, K. Luo, Construction of MWNT supported ultra-small Ag@MnO₂ nanoparticles for the ORR and Al-air batteries, Sustain. Energy Fuels 7 (14) (2023) 3276–3283, https://doi.org/ 10.1039/d3se00337i.
- [51] M. Wang, X. Zhuge, T. Liu, S. Jia, K. Luo, Y. Ren, A. Shahzad, X. Liu, Preparation of composite Single-Ion conductor membrane and its application in Lithium–Oxygen battery, Adv. Energy Sustain. Res. (2023) 2300111, https://doi.org/10.1002/ aesr.202300111.
- [52] Y.Y. Wang, M.M. Zhao, Q.X. Zhao, Q. Li, H. Pang, Facile synthesis of silver nanowire-zeolitic imidazolate framework 67 composites as high-performance bifunctional oxygen catalysts, Nanoscale 10 (33) (2018) 15755–15762, https:// doi.org/10.1039/c8nr03443e.
- [53] Z. Li, W.J. Kang, H. Liu, X.W. Du, F. Wang, Y. Song, Y. Liu, D.L. Sun, F. Fang, Ag anchored atomically around nanopores of porous Co(OH)₂ for efficient bifunctional oxygen catalysis, Adv. Funct. Mater. 33 (34) (2023) 2301947, https://doi.org/10.1002/adfm.202301947.
- [54] A. Ashok, A. Kumar, M.A. Matin, F. Tarlochan, Synthesis of highly efficient bifunctional Ag/Co₃O₄ catalyst for oxygen reduction and oxygen evolution reactions in alkaline medium, ACS Omega 3 (7) (2018) 7745–7756, https://doi. org/10.1021/acsomega.8b00799.
- [55] D. Li, C. Hu, Y. Luo, G. Zhu, Q. Li, Z. Luo, K. Luo, One-pot synthesis of amphiphilic janus gold nanoparticles with d-penicillamine and benzyl mercaptan ligands by toluene/water emulsion reaction, Appl. Surf. Sci. 475 (2019) 615–620, https://doi. org/10.1016/j.apsusc.2019.01.021.
- [56] J. Huo, X. Cao, Y. Tian, L. Li, J. Qu, Y. Xie, X. Nie, Y. Zhao, J. Zhang, H. Liu, Atomically dispersed mn atoms coordinated with n and o within an N-doped porous carbon framework for boosted oxygen reduction catalysis, Nanoscale 15 (11) (2023) 5448–5457, https://doi.org/10.1039/d2nr06096e.
- [57] H.D. Xu, J. Yang, R.Y. Ge, J.J. Zhang, Y. Li, M.Y. Zhu, L.M. Dai, S. Li, W.X. Li, Carbon-based bifunctional electrocatalysts for oxygen reduction and oxygen evolution reactions: optimization strategies and mechanistic analysis, J. Energy Chem. 71 (2022) 234–265, https://doi.org/10.1016/j.jechem.2022.03.022.

- [58] H. Zhang, P. Li, H.C. Zhou, J.M. Xu, Q.F. Jiang, J.H.L. Hadden, Y.Y. Wang, M. N. Wang, S.L. Chen, F. Xie, J. Riley, Unravelling the synergy of oxygen vacancies and gold nanostars in hematite for the electrochemical and photoelectrochemical oxygen evolution reaction, Nano Energy 94 (2022) 106968, https://doi.org/10.1016/j.nanoen.2022.106968.
- [59] S. Zhu, J. Wang, H. Li, J. Cai, Y. Li, J. Hu, Y. He, Y. Zhou, NiFe layered double hydroxide nanosheets anchored on cobalt nanocrystal matrixes as electrocatalysts for oxygen evolution, ACS Appl. Nano Mater. 5 (9) (2022) 13047–13054, https:// doi.org/10.1021/acsanm.2c02844.
- [60] J. Xue, S. Deng, R. Wang, Y. Li, Efficient synergistic effect of trimetallic organic frameworks derived as bifunctional catalysis for the rechargeable zinc-air flow battery, Carbon 205 (2023) 422–434, https://doi.org/10.1016/j. carbon.2023.01.034.
- [61] Y. Chen, T. He, Q. Liu, Y. Hu, H. Gu, L. Deng, H. Liu, Y. Liu, Y.-N. Liu, Y. Zhang, S. Chen, X. Ouyang, Highly durable iron single-atom catalysts for low-temperature zinc-air batteries by electronic regulation of adjacent iron nanoclusters, Appl. Catal. B Environ. 323 (2023) 122163, https://doi.org/10.1016/j. apcatb.2022.122163.
- [62] C.C. Cheng, P.Y. Cheng, C.L. Huang, D.S. Raja, Y.J. Wu, S.Y. Lu, Gold nanocrystal decorated trimetallic metal organic frameworks as high performance electrocatalysts for oxygen evolution reaction, Appl. Catal. B Environ. 286 (2021) 119916, https://doi.org/10.1016/j.apcatb.2021.119916.
- [63] J. Zhang, J. Liu, L. Xi, Y. Yu, N. Chen, S. Sun, W. Wang, K.M. Lange, B. Zhang, Single-Atom Au/NiFe layered double hydroxide electrocatalyst: probing the origin of activity for oxygen evolution reaction, J. Am. Chem. Soc. 140 (11) (2018) 3876–3879, https://doi.org/10.1021/jacs.8b00752.
- [64] M.O. Aydogdu, A. Delbusso, M. Edirisinghe, A battery powered approach to pressurised spinning: Introducing the sustainability concept and shaping the future of fibre production methodologies, Appl. Energy. 397 (2025) 126331, https://doi. org/10.1016/j.apenergy.2025.126331.